GEOPHYSICS, VOL. 84, NO. 5 (SEPTEMBER-OCTOBER 2019); P. 1–11, 15 FIGS., 2 TABLES.
10.1190/GEO2018-0732.1

Nearly perfectly matched layer absorber for viscoelastic wave equations

Enjiang Wang[1], José M. Carcione[2], Jing Ba[1], Mamdoh Alajmi[3], and Ayman N. Qadrouh[3]

ABSTRACT

We have applied the nearly perfectly matched layer (N-PML) absorber to the viscoelastic wave equation based on the Kelvin-Voigt and Zener constitutive equations. In the first case, the stress-strain relation has the advantage of not requiring additional physical field (memory) variables, whereas the Zener model is more adapted to describe the behavior of rocks subject to wave propagation in the whole frequency range. In both cases, eight N-PML artificial memory variables are required in the absorbing strips. The modeling simulates 2D waves by using two different approaches to compute the spatial derivatives, generating different artifacts from the boundaries, namely, 16th-order finite differences, where reflections from the boundaries are expected, and the staggered Fourier pseudospectral method, where wraparound occurs. The time stepping in both cases is a staggered second-order finite-difference scheme. Numerical experiments demonstrate that the N-PML has a similar performance as in the lossless case. Comparisons with other approaches (S-PML and C-PML) are carried out for several models, which indicate the advantages and drawbacks of the N-PML absorber in the anelastic case.

INTRODUCTION

Wave modeling is a valuable tool for seismic interpretation and is an essential part of inversion algorithms. Most problems regarding environmental geophysics, seismic exploration, earthquake seismology, and nondestructive testing of materials require the use of full-wave modeling methods based on model discretization (a mesh). However, the finite nature of the discretized models generates reflections and/or wraparound from the edges of the mesh, and damping has to be implemented on these boundaries in the form of absorbing strips. This is also a common problem in laboratory experiments (Krawczyk et al., 2013; Bodet et al., 2014).

Kosloff and Kosloff (1986) introduce a modification of the wave equation inside the absorbing strips, where the solution is a wave traveling without dispersion, but whose amplitude decreases with distance at a frequency-independent rate. A traveling pulse will thus diminish in amplitude without a change of shape. On the other hand, the split perfectly matched layer (S-PML) method has been proposed by Bérenger (1994) as an absorbing boundary condition (ABC) for electromagnetic waves. Later, the method has been modified to improve its performance at grazing angles (convolutional C-PML) (e.g., Komatitsch and Martin, 2007). The method has been widely used in finite-difference (FD) and finite-element methods. Carcione and Kosloff (2013) reinterpret all of the PML methods in terms of mechanical models and show their relationships in the time and frequency domains. The S-PML and Kosloff and Kosloff methods are based on a Maxwell viscoelastic model, whereas the C-PML is based on the well-known memory-variable equations used to model wave propagation in anelastic media (Carcione, 2014). Many high-order ABC methods (Bécache et al., 2010; Etienne et al., 2010; Rabinovich et al., 2010; Hagstrom et al., 2012) and hybrid ABCs (Liu and Sen, 2010, 2012; Ren and Liu, 2013) have also been developed, in the time and frequency domains, for modeling acoustic and elastic equations.

As shown by Chen (2011, 2012), the so-called nearly perfect matched layer (N-PML) differs from the previous PML models by using fewer auxiliary variables and ordinary differential equations, while having the same performance. He implements the method for the 2D isotropic elastic wave equation and clearly shows its efficiency compared with the previous PML methods. Moreover, Hu and Cummer (2004) and Hu et al. (2007) show that despite the word "nearly," the N-PML absorber is analytically (exactly) equivalent to the standard PML in Cartesian coordinates for 1D, 2D, and 3D problems. The difference between the two PML forms is only in implementation, the N-PML being particularly simple to code because it retains the form of the regular medium partial difference

Manuscript received by the Editor 24 October 2018; revised manuscript received 26 March 2019; published ahead of production 28 May 2019.
[1]Hohai University, School of Earth Sciences and Engineering, Nanjing 211100, China. E-mail: jba@hhu.edu.cn (corresponding author).
[2]Hohai University, School of Earth Sciences and Engineering, Nanjing 211100, China and Istituto Nazionale di Oceanografia e di Geofisica Sperimentale (OGS), Borgo Grotta Gigante 42c, 34010 Sgonico, Trieste, Italy.
[3]SAC — KACST, PO Box 6086, Riyadh 11442, Saudi Arabia.

equations even in lossy and anisotropic materials and does so with a minimum of auxiliary variables and additional computation. Recently, Lai and Minkoff (2017) evidence additional advantages of the method, such as that the equations are the same as the original governing equations and code parallelization remains unaffected.

The purpose of the present work is to show how to implement the N-PML absorber in anelastic wave equations based on the Kelvin-Voigt (KV) and Zener mechanical models, two of the most used mechanical models to describe attenuation and velocity dispersion in solids (e.g., Carcione and Helle, 2004; Carcione et al., 2004). The method is illustrated in two dimensions, but extension to the 3D space is straightforward. The KV model requires the calculations of additional spatial derivatives and avoids the viscoelastic memory variables (Carcione et al., 2004), saving computer memory, whereas the Zener model is more physical to describe wave propagation in solids, but it requires viscoelastic memory variables. In both cases, eight additional artificial memory variables for the absorbing strips are required (2D space), which are based on the Maxwell mechanical model. The equations are solved with a second-order FD scheme for time stepping and 16th-order staggered FD to compute the spatial derivatives (e.g., Virieux, 1986), which is the same algorithm used by Chen (2011, 2012), but here we use a more accurate spatial differentiation. In this case, reflections from the mesh boundaries are expected. In addition, we solve the problem using the staggered Fourier pseudospectral method to compute the spatial derivatives where the wavefield wraparound occurs (Carcione, 1999).

KELVIN-VOIGT MODEL

Equation of motion

The equations of momentum conservation can be expressed as

$$\rho \ddot{u}_i = \frac{\partial \sigma_{ij}}{\partial x_j} + f_i, \tag{1}$$

where ρ is the density, u_i are the displacement components, σ_{ij} denote the stress components, and f_j are the body forces. A dot above a variable denotes time differentiation, and the Einstein convention for repeated indices is used.

The stress-strain relations for a KV solid are a simple generalization of those for 1D media (Carcione et al., 2004; Carcione, 2014). They are

$$\sigma_{ij} = (\lambda\theta + \lambda'\dot{\theta})\delta_{ij} + 2\mu\epsilon_{ij} + 2\mu'\dot{\epsilon}_{ij}, \tag{2}$$

where λ and μ are the Lamé constants, λ' and μ' are the corresponding anelastic parameters,

$$\epsilon_{ij} = \frac{1}{2}\left(\frac{\partial u_i}{\partial x_j} + \frac{\partial u_j}{\partial x_i}\right) \tag{3}$$

are the strain components,

$$\theta = \frac{\partial u_i}{\partial x_i}, \tag{4}$$

and δ_{ij} is Kronecker's delta.

Following Carcione et al. (2004), the anelastic parameters can be obtained from the quality factors at a given (reference) frequency ω_0 as

$$\lambda' = \frac{1}{\omega_0}\left(\frac{E}{Q_P} - \frac{2\mu}{Q_S}\right) \quad \text{and} \quad \mu' = \frac{\mu}{\omega_0 Q_S}, \tag{5}$$

where Q_P and Q_S are the quality factors at $\omega = \omega_0$ and $E = \lambda + 2\mu$ and μ are the moduli at $\omega = 0$. In terms of velocities, $E = \rho V_{\mathrm{P}}^2$ and $\mu = \rho V_{\mathrm{S}}^2$, where V_{P} and V_{S} are the low-frequency limit phase velocities.

Velocity-stress formulation

The 3D particle velocity-stress formulation has been proposed in Carcione et al. (2004). The 2D case is as follows. Define the quantities

$$\Pi_x = \frac{1}{\rho}\left(\frac{\partial \sigma_{xx}}{\partial x} + \frac{\partial \sigma_{xz}}{\partial z} + f_x\right), \tag{6}$$

$$\Pi_z = \frac{1}{\rho}\left(\frac{\partial \sigma_{xz}}{\partial x} + \frac{\partial \sigma_{zz}}{\partial z} + f_z\right), \tag{7}$$

$$\psi = \frac{\partial \Pi_x}{\partial x} + \frac{\partial \Pi_z}{\partial z} \quad \text{and} \quad \vartheta = \frac{\partial v_x}{\partial x} + \frac{\partial v_z}{\partial z}. \tag{8}$$

Then, the KV momentum and stress-strain relations equations are

$$\dot{v}_x = \Pi_x, \dot{v}_z = \Pi_z \tag{9}$$

and

$$\dot{\sigma}_{xx} = \lambda\vartheta + \lambda'\psi + 2\mu\frac{\partial v_x}{\partial x} + 2\mu'\frac{\partial \Pi_x}{\partial x}, \tag{10}$$

$$\dot{\sigma}_{zz} = \lambda\vartheta + \lambda'\psi + 2\mu\frac{\partial v_z}{\partial z} + 2\mu'\frac{\partial \Pi_z}{\partial z}, \tag{11}$$

$$\dot{\sigma}_{xz} = \mu\left(\frac{\partial v_x}{\partial z} + \frac{\partial v_z}{\partial x}\right) + \mu'\left(\frac{\partial \Pi_x}{\partial z} + \frac{\partial \Pi_z}{\partial x}\right), \tag{12}$$

respectively.

Equations 9–12 constitute the velocity-stress formulation for the KV model in 2D space. The extra cost to avoid memory-variable requirements is the calculation of additional spatial derivatives corresponding to the acceleration components.

N-PML equations

In the N-PML method, all of the variables in the spatial derivatives are rescaled by a complex damping function, e.g.

$$\frac{\partial v_x}{\partial x} \rightarrow \frac{\partial w_x}{\partial x}, \quad w_x = \frac{v_x}{s_x}, \quad s_x = 1 + \frac{d_x}{i\omega}, \tag{13}$$

where ω is the angular frequency and d_x is a damping parameter (e.g., Chen, 2011). The damper s_x is equivalent to a Maxwell model (Carcione and Kosloff, 2013). In the time domain, equation 13 is

$$w_x = v_x * \frac{1}{s_x} = v_x * \partial_t[H(t)\exp(-d_x t)], \tag{14}$$

where H is the Heaviside function. Let us find an equation for w_x (it is similar to a memory-variable equation, e.g., Carcione, 2014). Differentiating equation 14, we easily obtain

$$\dot{w}_x = \dot{v}_x - d_x w_x. \tag{15}$$

However, we have to distinguish between

$$\partial_x\left(\frac{v_x}{s_x}\right) \quad \text{and} \quad \partial_z\left(\frac{v_x}{s_z}\right), \tag{16}$$

so we redefine

$$w_{xx} = \frac{v_x}{s_x} \quad \text{and} \quad w_{zx} = \frac{v_x}{s_z}, \tag{17}$$

where the first subindex on the left side corresponds to the spatial derivative.

We rescale the primary unknown variables $[v_x, v_z, \sigma_{xx}, \sigma_{zz}, \sigma_{xz}]$. Considering equations 9–12, the complete set of artificial memory-variable equations in the absorbing strips is

$$\begin{cases} \dot{w}_{xx} = \dot{v}_x - d_x w_{xx}, \\ \dot{w}_{zx} = \dot{v}_x - d_z w_{zx}, \\ \dot{w}_{xz} = \dot{v}_z - d_x w_{xz}, \\ \dot{w}_{zz} = \dot{v}_z - d_z w_{zz}, \\ \dot{\tau}_{xx} = \dot{\sigma}_{xx} - d_x \tau_{xx}, \\ \dot{\tau}_{zz} = \dot{\sigma}_{zz} - d_z \tau_{zz}, \\ \dot{\tau}_{xxz} = \dot{\sigma}_{xz} - d_x \tau_{xxz}, \\ \dot{\tau}_{zxz} = \dot{\sigma}_{xz} - d_z \tau_{zxz}, \end{cases} \tag{18}$$

where

$$w_{xx} = \frac{v_x}{s_x}, \quad w_{zx} = \frac{v_x}{s_z}, \quad w_{xz} = \frac{v_z}{s_x}, \quad w_{zz} = \frac{v_z}{s_z},$$
$$\tau_{xx} = \frac{\sigma_{xx}}{s_x}, \quad \tau_{xxz} = \frac{\sigma_{xz}}{s_x}, \quad \tau_{zxz} = \frac{\sigma_{xz}}{s_z}, \quad \tau_{zz} = \frac{\sigma_{zz}}{s_z}. \tag{19}$$

The equation of motion 9 is replaced by

$$\begin{cases} \dot{v}_x = \bar{\Pi}_x = \frac{1}{\rho}\left(\frac{\partial \tau_{xx}}{\partial x} + \frac{\partial \tau_{zxz}}{\partial z} + f_x\right), \\ \dot{v}_z = \bar{\Pi}_z = \frac{1}{\rho}\left(\frac{\partial \tau_{xxz}}{\partial x} + \frac{\partial \tau_{zz}}{\partial z} + f_z\right), \end{cases} \tag{20}$$

and the stress-strain relations 10–12 by

$$\dot{\sigma}_{xx} = \lambda\bar{\vartheta} + \lambda'\bar{\psi} + 2\mu\frac{\partial w_{xx}}{\partial x} + 2\mu'\frac{\partial \bar{\Pi}_x}{\partial x}, \tag{21}$$

$$\dot{\sigma}_{zz} = \lambda\bar{\vartheta} + \lambda'\bar{\psi} + 2\mu\frac{\partial w_{zz}}{\partial z} + 2\mu'\frac{\partial \bar{\Pi}_z}{\partial z}, \tag{22}$$

$$\dot{\sigma}_{xz} = \mu\left(\frac{\partial w_{zx}}{\partial z} + \frac{\partial w_{xz}}{\partial x}\right) + \mu'\left(\frac{\partial \bar{\Pi}_x}{\partial z} + \frac{\partial \bar{\Pi}_z}{\partial x}\right). \tag{23}$$

To obtain a velocity-stress formulation, we have to replace equations 20–23 into equation 18, obtaining

$$\begin{cases} \dot{w}_{xx} = \bar{\Pi}_x - d_x w_{xx}, \\ \dot{w}_{zx} = \bar{\Pi}_x - d_z w_{zx}, \\ \dot{w}_{xz} = \bar{\Pi}_z - d_x w_{xz}, \\ \dot{w}_{zz} = \bar{\Pi}_z - d_z w_{zz}, \\ \dot{\tau}_{xx} = \lambda\bar{\vartheta} + \lambda'\bar{\psi} + 2\mu\frac{\partial w_{xx}}{\partial x} + 2\mu'\frac{\partial \bar{\Pi}_x}{\partial x} - d_x\tau_{xx}, \\ \dot{\tau}_{zz} = \lambda\bar{\vartheta} + \lambda'\bar{\psi} + 2\mu\frac{\partial w_{zz}}{\partial z} + 2\mu'\frac{\partial \bar{\Pi}_z}{\partial z} - d_z\tau_{zz}, \\ \dot{\tau}_{xxz} = \mu\left(\frac{\partial w_{zx}}{\partial z} + \frac{\partial w_{xz}}{\partial x}\right) + \mu'\left(\frac{\partial \bar{\Pi}_x}{\partial z} + \frac{\partial \bar{\Pi}_z}{\partial x}\right) - d_x\tau_{xxz}, \\ \dot{\tau}_{zxz} = \mu\left(\frac{\partial w_{zx}}{\partial z} + \frac{\partial w_{xz}}{\partial x}\right) + \mu'\left(\frac{\partial \bar{\Pi}_x}{\partial z} + \frac{\partial \bar{\Pi}_z}{\partial x}\right) - d_z\tau_{zxz}. \end{cases} \tag{24}$$

Then, we solve equations 20–24, with d_x and d_z different from zero only in the absorbing strips.

In the 2D N-PML formulation, we pass from $[v_x, v_z, \sigma_{xx}, \sigma_{zz}, \sigma_{xz}]$ (5 unknown variables) to $[v_x, v_z, w_{xx}, w_{zz}, w_{xz}, w_{zx}, \sigma_{xx}, \sigma_{zz}, \sigma_{xz}, \tau_{xx}, \tau_{zz}, \tau_{xxz}, \tau_{zxz}]$ (13 variables).

Parameters d_x and d_z are of the form

$$d_x = d_0(x/L)^N, d_0 = -(N+1)v_{\max}\log(R)/(2L), \tag{25}$$

where L is the length of the strip, $N = 2$, $R = 0.001$, and $v_{\max}$ is the maximum velocity ($x = 0$ is the entrance to the strip) (Komatitsch and Martin, 2007; Chen, 2011).

ZENER MODEL

The equations for the Zener model, based on the physical memory variables (Carcione and Helle, 2004), are given by the equations of momentum conservation (equation 9), the constitutive equations:

$$\dot{\sigma}_{xx} = \lambda\vartheta + 2\mu\frac{\partial v_x}{\partial x} + \lambda e_1 + \mu(e_1 + e_2), \tag{26}$$

$$\dot{\sigma}_{zz} = \lambda\vartheta + 2\mu\frac{\partial v_z}{\partial z} + \lambda e_1 + \mu(e_1 - e_2), \tag{27}$$

$$\dot{\sigma}_{xz} = \mu\left(\frac{\partial v_x}{\partial z} + \frac{\partial v_z}{\partial x} + e_3\right), \tag{28}$$

where e_1, e_2, and e_3 are the memory variables, and λ and μ are the unrelaxed (high-frequency) Lamé constants, respectively, and the memory-variable equations

$$\dot{e}_1 = \left(\frac{1}{\tau_\epsilon^{(1)}} - \frac{1}{\tau_\sigma^{(1)}}\right)\vartheta - \frac{e_1}{\tau_\sigma^{(1)}}, \tag{29}$$

$$\dot{e}_2 = \left(\frac{1}{\tau_\epsilon^{(2)}} - \frac{1}{\tau_\sigma^{(2)}}\right)\left(\frac{\partial v_x}{\partial x} - \frac{\partial v_z}{\partial z}\right) - \frac{e_2}{\tau_\sigma^{(2)}}, \tag{30}$$

$$\dot{e}_3 = \left(\frac{1}{\tau_\epsilon^{(2)}} - \frac{1}{\tau_\sigma^{(2)}}\right)\left(\frac{\partial v_x}{\partial z} + \frac{\partial v_z}{\partial x}\right) - \frac{e_3}{\tau_\sigma^{(2)}}, \tag{31}$$

where $\tau_\sigma^{(\nu)}$ and $\tau_\epsilon^{(\nu)}$ are the material relaxation times, corresponding to the dilatational ($\nu = 1$) and shear ($\nu = 2$) deformations. The relaxation times can be expressed as

$$\tau_\epsilon^{(\nu)} = \frac{\tau_0}{Q_\nu}\left(\sqrt{Q_\nu^2 + 1} + 1\right),$$
$$\tau_\sigma^{(\nu)} = \tau_\epsilon^{(\nu)} - \frac{2\tau_0}{Q_\nu}, \tag{32}$$

where τ_0 is a relaxation time, such that $1/\tau_0$ is the center frequency of the relaxation peak and Q_ν are the minimum quality factors. We assume $\tau_0\omega_0 = 1$, where ω_0 is a reference frequency that can be the dominant frequency of the source. The quality factor Q_1, associated with the bulk modulus, is obtained from the relation:

$$\frac{1+\sigma}{Q_1} = \frac{3(1-\sigma)}{Q_P} - \frac{2(1-2\sigma)}{Q_2},$$
$$\sigma = \frac{(V_\mathrm{P}/V_\mathrm{S})^2 - 2}{2(V_\mathrm{P}/V_\mathrm{S})^2 - 2}, \tag{33}$$

where σ is the Poisson's ratio, and Q_P is the P-wave quality factor, whereas the S-wave quality factor is $Q_S = Q_2$. Here, V_P and V_S are the unrelaxed (infinite-frequency) velocities.

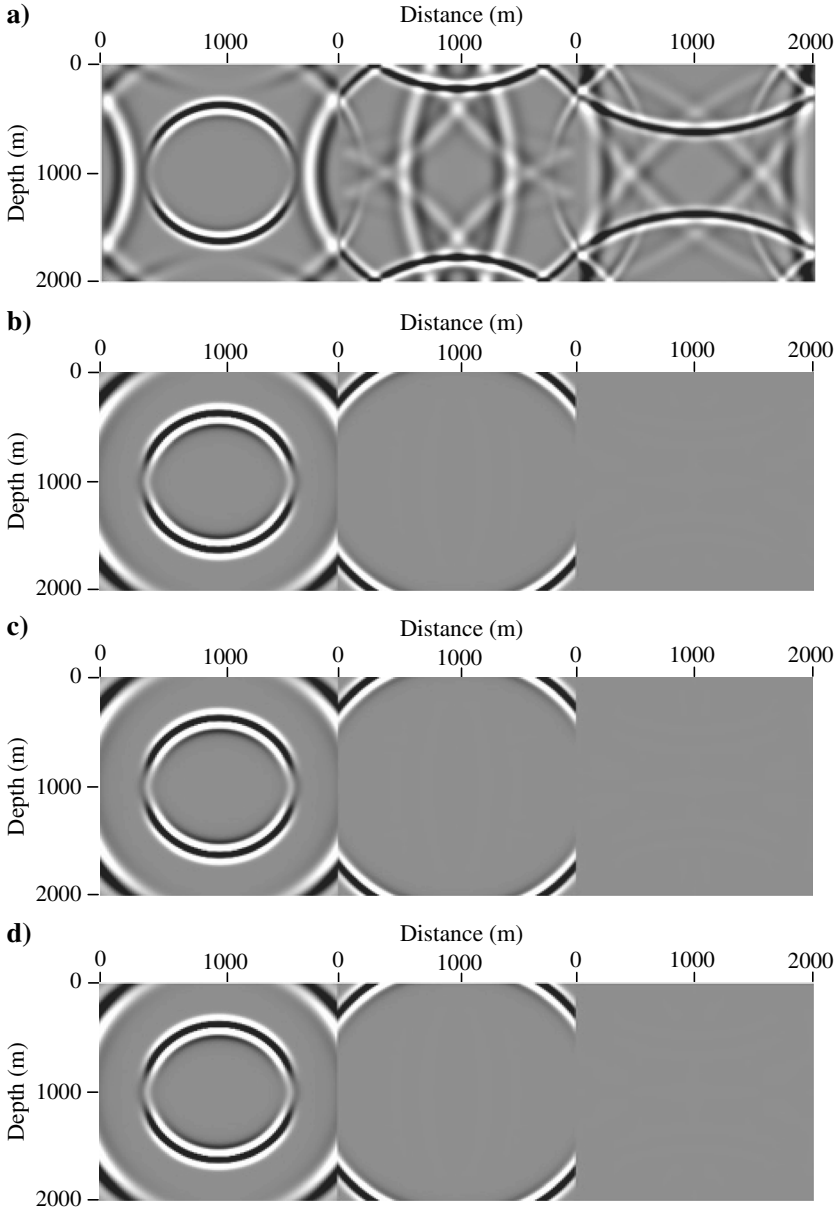

Figure 1. Snapshots at three propagation times (0.4, 0.7, and 0.9 s) (a) without absorbing layers, (b) with C-PML ABC, (c) with N-PML ABC, and (d) with S-PML ABC, based on the KV stress-strain relation.

Table 1. Field variables of the ABCs.

Model	S-PML		N-PML		C-PML	
	Number	Variables	Number	Variables	Number	Variables
KV	15	$v_x, v_{xx}, v_{xz}, v_z, v_{zx}, v_{zz}, \sigma_{xx}, \sigma_{xxx}, \sigma_{xxz}, \sigma_{zz}, \sigma_{zzx}, \sigma_{zzz}, \sigma_{xz}, \sigma_{xzx}, \sigma_{xzz}$	13	$v_x, v_z, \sigma_{xx}, \sigma_{zz}, \sigma_{xz}, w_{xx}, w_{zx}, w_{xz}, w_{zz}, \tau_{xx}, \tau_{zz}, \tau_{xxz}, \tau_{zxz}$	17	$v_x, v_z, \sigma_{xx}, \sigma_{zz}, \sigma_{xz}, \psi_x(\sigma_{xx}), \psi_z(\sigma_{xz}), \psi_x(\sigma_{xz}), \psi_z(\sigma_{zz}), \psi_x(v_x), \psi_z(v_z), \psi_x(v_z), \psi_z(v_x), \psi_x(\Pi_x), \psi_z(\Pi_z), \psi_x(\Pi_z), \psi_z(\Pi_x)$
Zener	24	$v_x, v_{xx}, v_{xz}, v_z, v_{zx}, v_{zz}, \sigma_{xx}, \sigma_{xxx}, \sigma_{xxz}, \sigma_{zz}, \sigma_{zzx}, \sigma_{zzz}, \sigma_{xz}, \sigma_{xzx}, \sigma_{xzz}, e_1, e_{1x}, e_{1z}, e_2, e_{2x}, e_{2z}, e_3, e_{3x}, e_{3z}$	16	$v_x, v_z, \sigma_{xx}, \sigma_{zz}, \sigma_{xz}, w_{xx}, w_{zx}, w_{xz}, w_{zz}, \tau_{xx}, \tau_{zz}, \tau_{xxz}, \tau_{zxz}, e_1, e_2, e_3$	16	$v_x, v_z, \sigma_{xx}, \sigma_{zz}, \sigma_{xz}, \psi_x(\sigma_{xx}), \psi_z(\sigma_{xz}), \psi_x(\sigma_{xz}), \psi_z(\sigma_{zz}), \psi_x(v_x), \psi_z(v_z), \psi_x(v_z), \psi_z(v_x), e_1, e_2, e_3$

N-PML equations

In this case, the N-PML equations are the momentum equation 20, the modified stress-strain relations

$$\dot{\sigma}_{xx} = \lambda\bar{\vartheta} + 2\mu\frac{\partial w_{xx}}{\partial x} + \lambda e_1 + \mu(e_1 + e_2), \tag{34}$$

$$\dot{\sigma}_{zz} = \lambda\bar{\vartheta} + 2\mu\frac{\partial w_{zz}}{\partial z} + \lambda e_1 + \mu(e_1 - e_2), \tag{35}$$

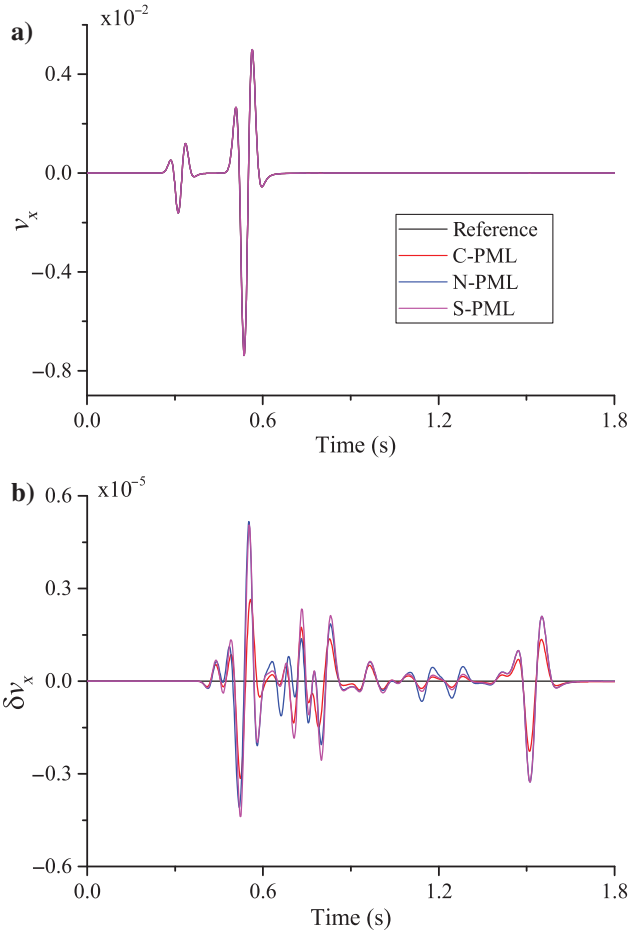

Figure 2. Waveform comparisons at (500, 250) m between the reference and numerical results, based on the KV model. The figure (b) shows the difference between the numerical results and the reference one.

Table 2. The CPU time (s).

Model	Geologic model	S-PML	N-PML	C-PML
KV	Homogeneous	146	140	142
	Marmousi	3295	3257	3302
Zener	Homogeneous	90	80	81
	Marmousi	1411	1253	1257

$$\dot{\sigma}_{xz} = \mu\left(\frac{\partial w_{zx}}{\partial z} + \frac{\partial w_{xz}}{\partial x} + e_3\right), \tag{36}$$

the modified memory-variable equations

$$\dot{e}_1 = \left(\frac{1}{\tau_\epsilon^{(1)}} - \frac{1}{\tau_\sigma^{(1)}}\right)\bar{\vartheta} - \frac{e_1}{\tau_\sigma^{(1)}}, \tag{37}$$

$$\dot{e}_2 = \left(\frac{1}{\tau_\epsilon^{(2)}} - \frac{1}{\tau_\sigma^{(2)}}\right)\left(\frac{\partial w_{xx}}{\partial x} - \frac{\partial w_{zz}}{\partial z}\right) - \frac{e_2}{\tau_\sigma^{(2)}}, \tag{38}$$

$$\dot{e}_3 = \left(\frac{1}{\tau_\epsilon^{(2)}} - \frac{1}{\tau_\sigma^{(2)}}\right)\left(\frac{\partial w_{zx}}{\partial z} + \frac{\partial w_{xz}}{\partial x}\right) - \frac{e_3}{\tau_\sigma^{(2)}}, \tag{39}$$

and the N-PML memory-variable equations, similar to equation 24, but including the physical memory variables

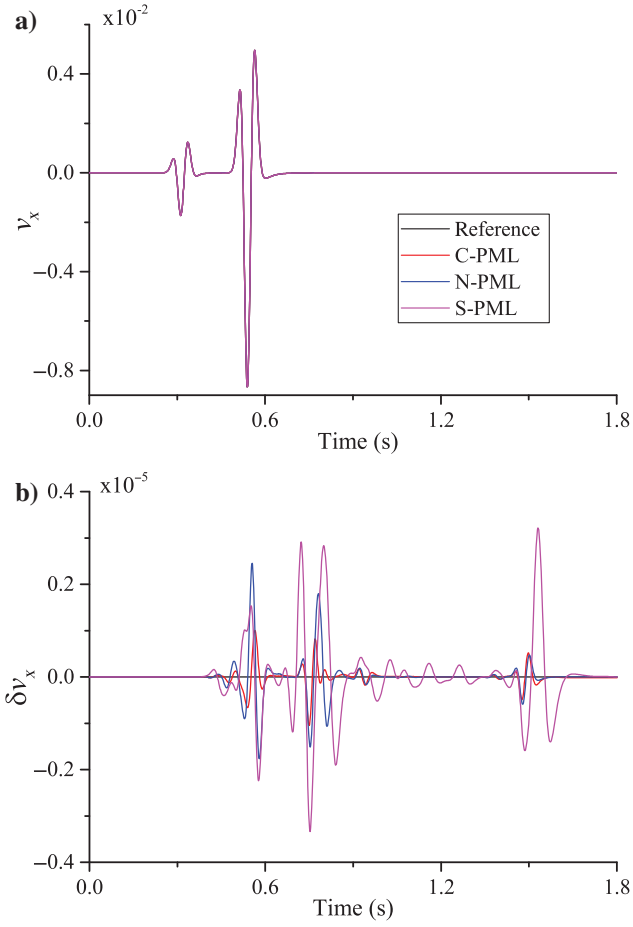

Figure 3. Waveform comparison at (500, 250) m between the reference and numerical results, based on the Zener model. The figure (b) plot shows the difference between the numerical results and the reference one.

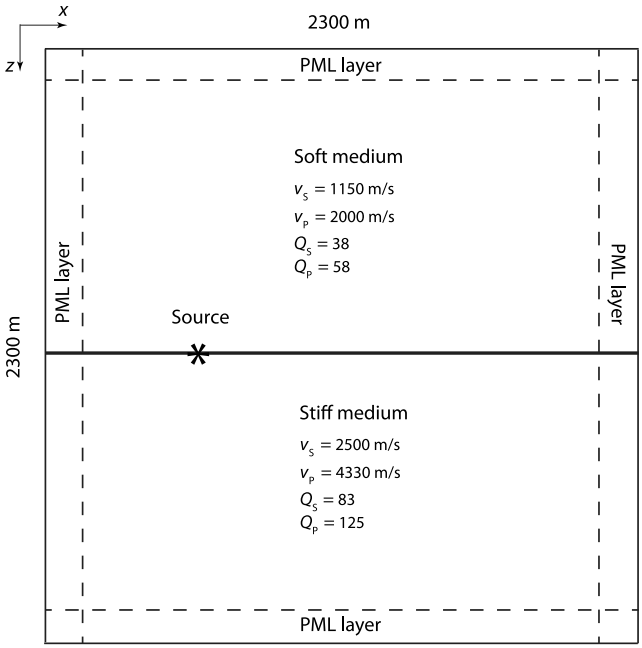

Figure 4. Model and source location (star), including the PML absorbing layers.

$$
\begin{cases}
\dot{w}_{xx} = \bar{\Pi}_x - d_x w_{xx}, \\
\dot{w}_{zx} = \bar{\Pi}_x - d_z w_{zx}, \\
\dot{w}_{xz} = \bar{\Pi}_z - d_x w_{xz}, \\
\dot{w}_{zz} = \bar{\Pi}_z - d_z w_{zz}, \\
\dot{\tau}_{xx} = \lambda\bar{\vartheta} + 2\mu\frac{\partial w_{xx}}{\partial x} + \lambda e_1 + \mu(e_1 + e_2) - d_x\tau_{xx}, \\
\dot{\tau}_{zz} = \lambda\bar{\vartheta} + 2\mu\frac{\partial w_{zz}}{\partial z} + \lambda e_1 + \mu(e_1 - e_2) - d_z\tau_{zz}, \\
\dot{\tau}_{xxz} = \mu\left(\frac{\partial w_{zx}}{\partial z} + \frac{\partial w_{xz}}{\partial x} + e_3\right) - d_x\tau_{xxz}, \\
\dot{\tau}_{zxz} = \mu\left(\frac{\partial w_{zx}}{\partial z} + \frac{\partial w_{xz}}{\partial x} + e_3\right) - d_z\tau_{zxz}.
\end{cases}
\tag{40}
$$

The number of field variables used by the three ABCs is shown in Table 1. Overall, the N-PML ABC involves the minimum number of variables. The differential equations are solved with a second-order FD algorithm in time, whose workflow is given in Appendix A.

EXAMPLES

Homogeneous model

A homogeneous model is implemented to compare the absorbing performances of the C-PML, N-PML, and S-PML ABCs. The reference solution, obtained with a much larger computational domain, is also shown. The model size is 2000×2000 m, and the grid size along the x- and z-axes is 10 m. A Ricker wavelet with a dominant frequency of 15 Hz is located at the center of the mesh. Absorbing layers with a thickness of 100 m, which corresponds to 10 grid cells, are implemented at the four boundaries. The medium properties are $V_P = 4000$ m/s, $V_S = 2000$ m/s, $\rho = 2100$ kg/m^3, $Q_P = 133$, and $Q_S = 67$.

Figure 1 shows snapshots at three propagation times, based on the KV model. All three methods effectively absorb the reflections. Waveform comparisons of the horizontal particle velocity component at (500, 250) m with the reference one are shown in Figure 2. It can be seen that the reflection amplitude is smaller by three orders of magnitude. The absorbing levels are comparable among the three methods. However, the N-PML ABC is more efficient in terms of computer time as shown in Table 2 because this ABC uses fewer field variables (see Table 1). A similar analysis based on the Zener model is given in Figure 3. The application of the N-PML ABC in this case effectively absorbs the boundary reflections, achieving the same performance of the C-PML ABC, but using fewer field variables for the KV model, and it outperforms the S-PML ABC. The run times displayed in Table 2 show that the N-PML ABC is much more efficient than the S-PML ABC, and is slightly more efficient than the C-PML ABC.

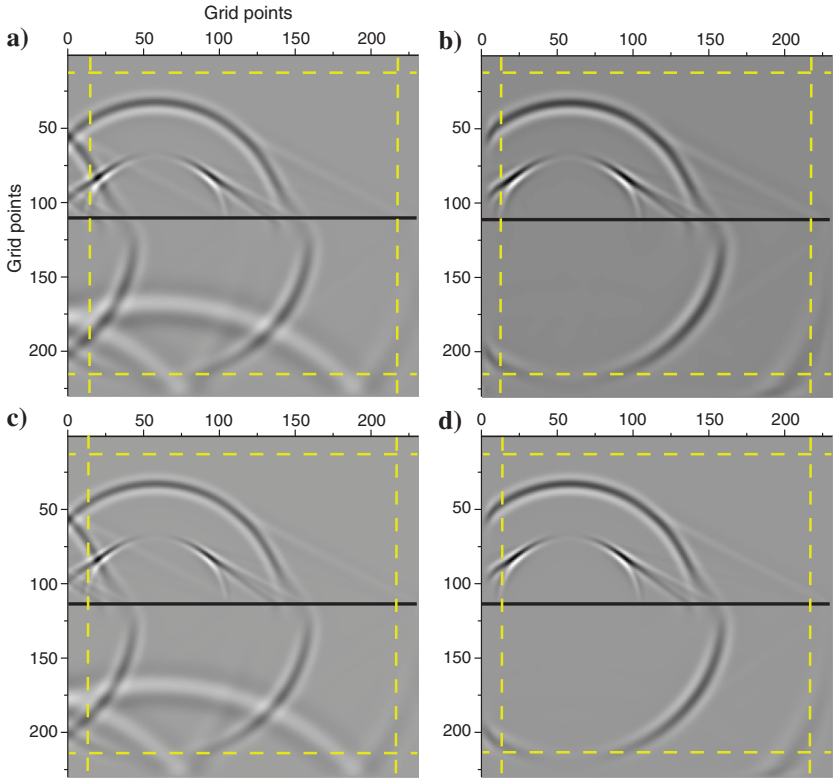

Figure 5. Snapshots of the vertical particle-velocity component at 500 ms. KV model, (a) without and (b) with N-PML absorbers. Zener model, (c) without and (d) with N-PML absorbers. The dashed yellow lines indicate the boundaries in the absorbing strips. The numerical scheme is (2, 16) accurate (FD).

Two-layer model

This example considers a soft half-space (1) overlying a stiff half-space (2) (see Figure 4),

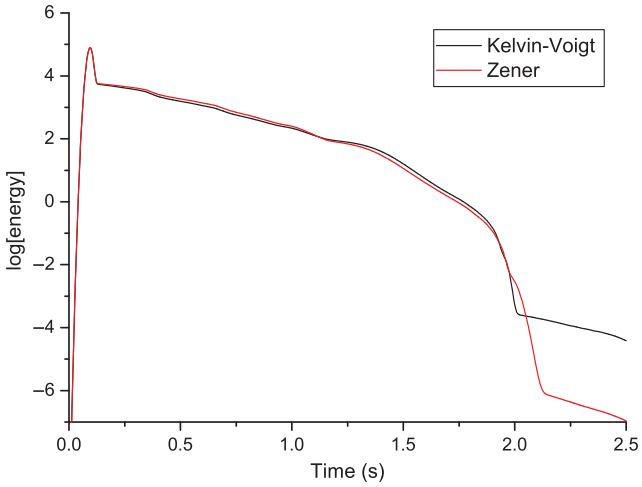

Figure 6. Decay of the total energy with time for the FD spatial differentiation.

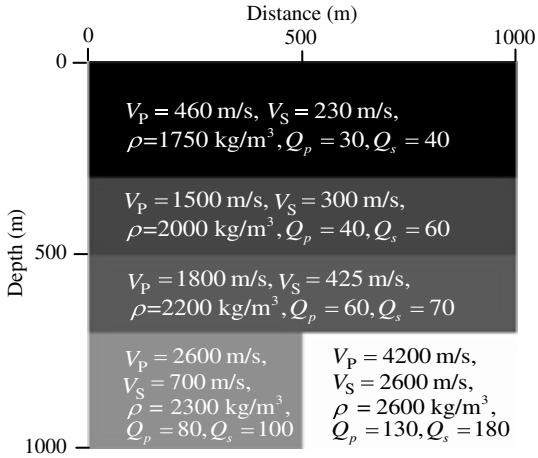

Figure 7. Heterogeneous model with high velocity contrasts and V_P/V_S ratio.

whose S-wave velocities are $V_{S1} = 1155$ m/s and $V_{S2} = 2500$ m/s, respectively. The other properties are obtained as $V_P = \sqrt{3}V_S$ (Poisson medium), $\rho = 0.31V_P^{1/4}$ (Gardner's relation, V_P given in m/s), $Q_S = V_S/(30\ \text{m/s})$ (V_S in m/s), $Q_P = (1/2)\gamma Q_S$, and $\gamma = (V_P/V_S)^2$. The simulations use a $n_x \times n_z = 231 \times 231$ mesh, with a uniform grid spacing $dx = dz = 10$ m. The 10 grid points of absorbing strips at the sides, top, and bottom of the model are used. The source is a vertical force (f_z), and its time history (a Ricker wavelet) is $h(t) = (a - 0.5)\exp(-a)$, $a = [\pi f_p(t - t_s)]^2$, $t_s = 1.4/f_p$, with $f_p = 15$ Hz, the source central frequency. The source is located at $(n_x/4, n_z/2)$. The length of the strips is $L = 100$ m; i.e., 10 grid points are used to damp the wavefield.

Figure 5 shows the snapshots of the vertical particle-velocity component at 500 ms for the KV model (Figure 5a and 5b) and for the Zener model (Figure 5c and 5d). Finite differences (staggered 16th-order) are used to compute the spatial derivatives. The right panels correspond to the simulations with the N-PML absorbers. The dashed yellow lines indicate the boundaries of the absorbing strips. As can be seen, the performance is optimal. To provide a quantitative verification of the field decay with time, we represent in Figure 6 the energy decay, where it can be appreciated that the energy has been lost in agreement with the values obtained by Chen (2011) in the lossless case.

Model with large velocity and V_P/V_S-ratio contrasts

In the presence of large velocity and V_P/V_S-ratio contrasts, the application of ABCs may introduce instability. A heterogeneous model with these characteristics (Oprsal and Zahradnik, 1999; Liu and Sen, 2012) is given in Figure 7, used to test the stability when applying the N-PML ABC. The model size is 1000×1000 m, and the grid spacing is 5 m. A Ricker wavelet with a dominant frequency of 8 Hz is located at $(500, 200)$ m, and the time step is 0.5 ms. Figure 8 displays the simulated v_x-component snapshots at three different propagation times using the KV model (Figure 8a) and the Zener model (Figure 8b). It is evident that the boundary reflections are effectively absorbed when the N-PML ABC is applied. The decay of the total energy with the time displayed in Figure 9 proves that the

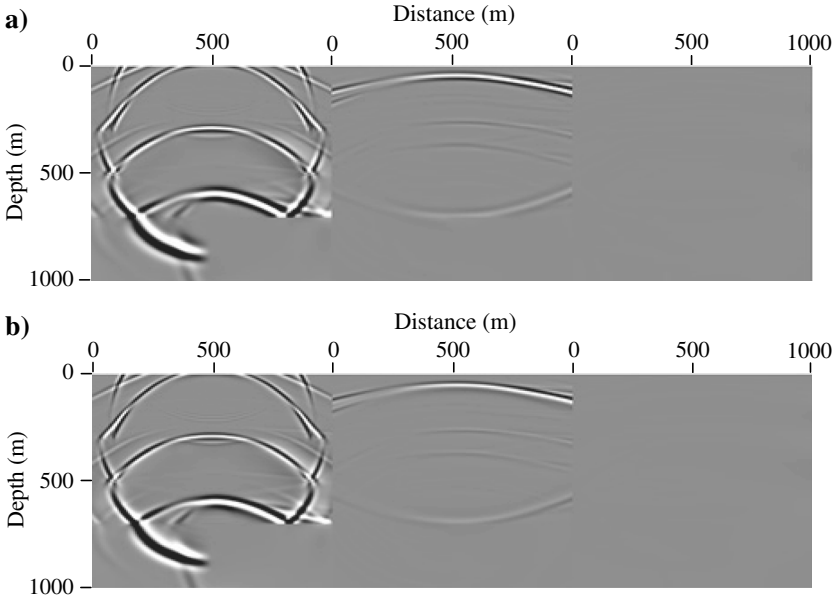

Figure 8. Snapshots of the v_x-component using the N-PML ABC, based on the (a) KV model and (b) Zener model. From left to right, the plots show snapshots at 2, 4, and 6 s.

modeling is stable for a long time, in this case 8 s, and the energy has effectively decayed for the KV and Zener models.

Marmousi model

To further test the effectiveness of the N-PML ABC for a complex model, we use the Marmousi one. The model size is 5010×3530 m, with a grid spacing of 10 m, and a time step of 0.8 ms. The source is a Ricker wavelet with a dominant frequency of 15 Hz, located at

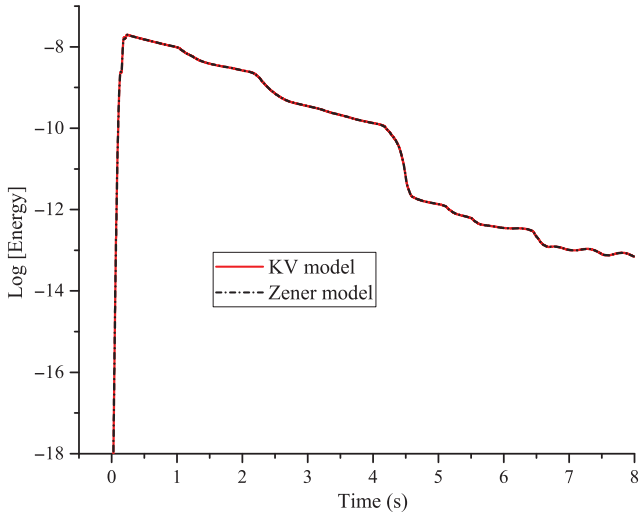

Figure 9. Decay of the total energy with propagation time for the heterogeneous model with high velocity contrasts and V_P/V_S ratio, using the N-PML absorber.

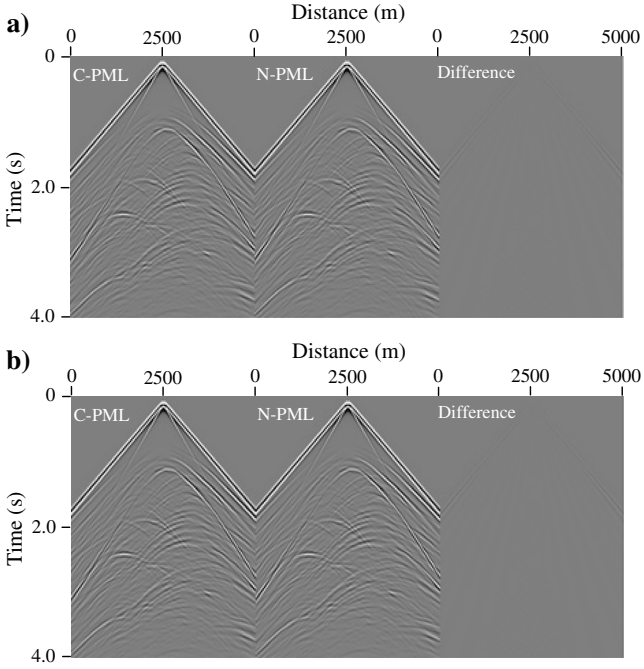

Figure 10. Seismic records of the v_x-component obtained with the C-PML and N-PML ABCs, corresponding to the (a) KV and (b) Zener models. In each figure, the rightmost panel exhibits the difference between the results generated from the C-PML and N-PML ABCs.

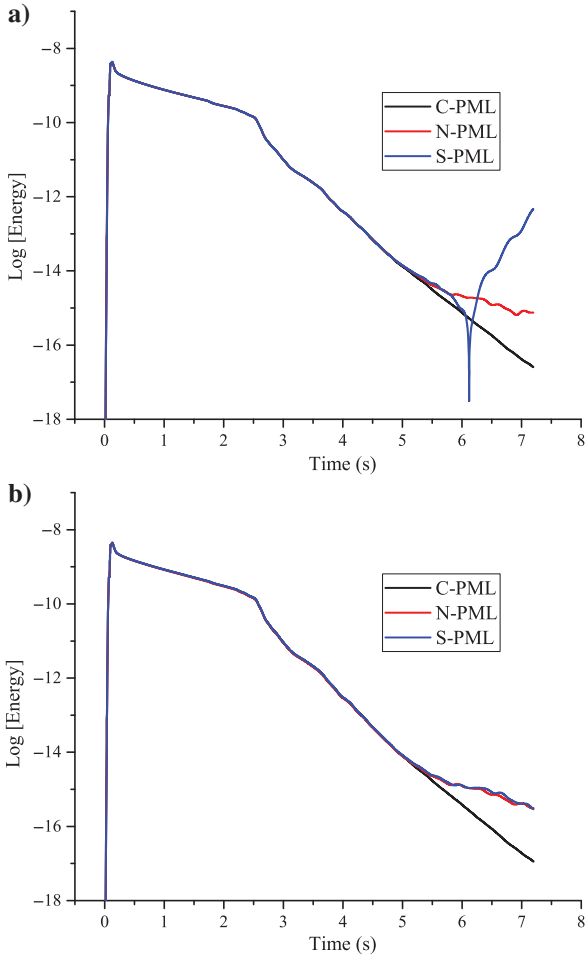

Figure 11. Decay of the total energy with propagation time for the Marmousi model, based on the (a) KV and (b) Zener models. Note that, the S-PML becomes unstable when the propagation time is larger than 7 s for the KV model.

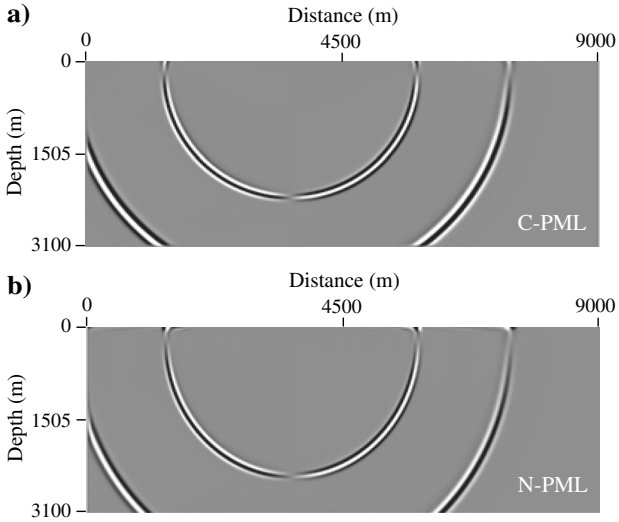

Figure 12. Snapshots at 2.0 s with the (a) C-PML and (b) N-PML ABCs, for the grazing incidence.

(2505, 50) m. For simplicity, we assume that the $Q_P = 50$ and $Q_S = 120$ everywhere. Absorbing layers with a thickness of 100 m, which corresponds to 10 grid cells, are implemented on all of the boundaries. Figure 10 shows the simulated records with the C-PML and N-PML ABCs, based on the KV and Zener models. It is evident that the boundaries reflections are effectively absorbed, and that the N-PML ABC achieves a comparable performance as the C-PML ABC. The small differences displayed in each figure can be attributed to the different computational errors.

Figure 11 shows the decay of the total energy with propagation time for the KV and Zener models. For times less than 5 s, the N-PML ABC exhibits a similar absorbing performance as the C-PML ABC. The S-PML ABC becomes unstable when the propagation time is larger than 7 s. Numerical tests show that the modeling is still stable for the N-PML and C-PML ABCs at 12 s. However, the C-PML ABC attenuates the reflections better than the N-PML ABC for time larger than 6 s.

Table 2 shows that, for a propagation time of 7.2 s, the application of the N-PML to the KV model takes less computational time than the C-PML and S-PML ABCs because it uses fewer field variables. The improvement when modeling with the 3D wave equation can be much more significant. For the Zener model, the N-PML and C-PML ABCs have a comparable computational time, much smaller than that of the S-PML ABC. Therefore, considering the balance between efficiency and absorbing accuracy, the N-PML ABCs for the KV model is superior to the C-PML one, and comparable for the Zener model.

Grazing incidence

At grazing incidence, the C-PML method has been developed to effectively absorb the reflections (Komatitsch and Martin, 2007; Martin and Komatitsch, 2009). Here, a simple example using the KV model is given to test the accuracy of the N-PML ABC at grazing incidence. The model size is 9000×3100 m, the grid spacing is 10 m, and the time step is 1 ms. The medium properties are $V_P = 2000$ m/s, $V_S = 1155$ m/s, $\rho = 2073$ kg/m^3, $Q_P = 58$, and $Q_S = 38$. The source is a Ricker wavelet with a 15 Hz dominant frequency, located at (3500, 100) m. The 10 N-PML grid points are used at all of the boundaries.

Figure 12 shows snapshots at 2 s, generated with the C-PML and N-PML ABCs. We observe that, compared with the C-PML ABC, the N-PML ABC exhibits a slight grazing reflection at the top, suggesting that the N-PML is slightly less accurate, which can also be seen in Figure 13 that shows the energy decay with time. The C-PML ABC absorbs the energy more efficiently for propagation times longer than 6 s. Therefore, at grazing incidence, the C-PML ABC is preferred to the N-PML ABC. However, the advantage of the N-PML ABC lies in requiring much less memory to store the variables, as shown in Table 1. This advantage is much more significant for the 3D modeling case, with a further decrease in computational time, for the KV and Zener models.

Pseudospectral modeling

Using the same two-layer model displayed in Figure 4, we further discuss the application of the N-PML ABC when using the Fourier pseudospectral method to compute the spatial derivatives. In this

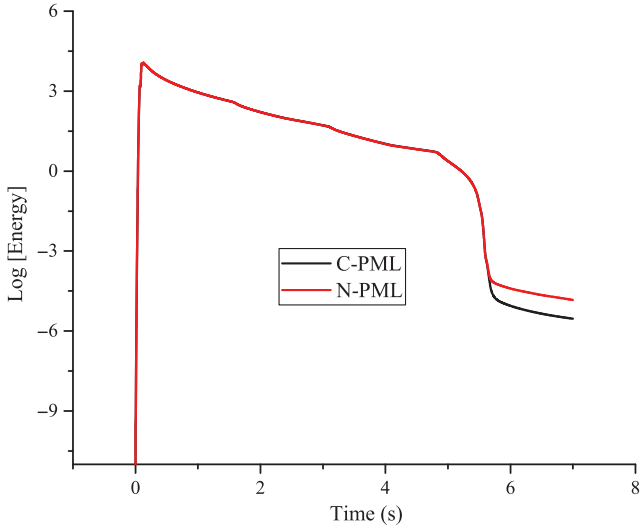

Figure 13. Decay of the total energy with propagation time for the grazing-incidence problem, corresponding to the KV model.

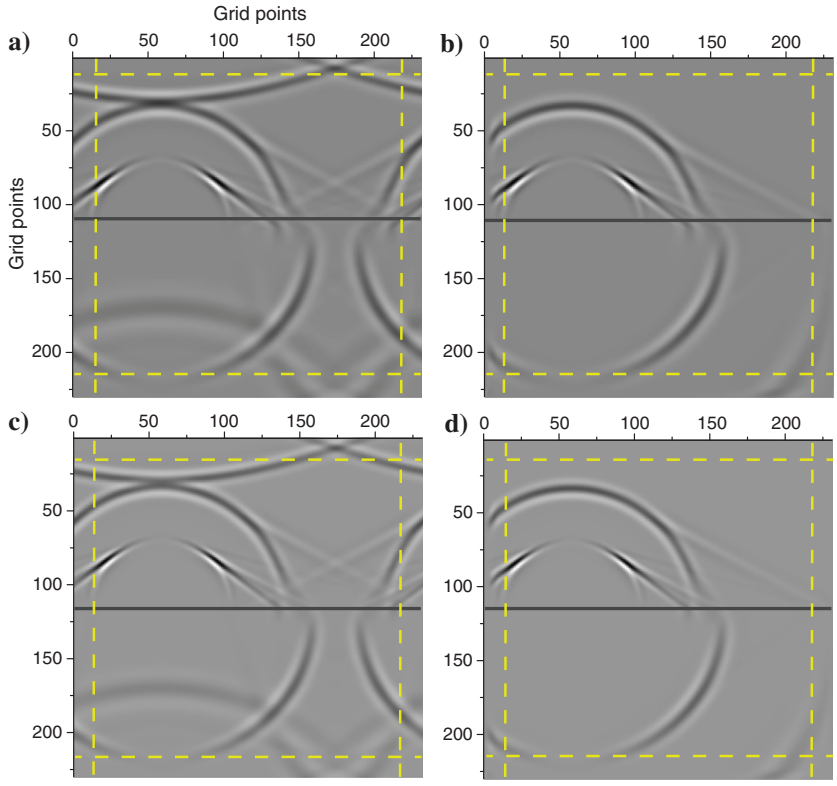

Figure 14. Snapshots of the vertical particle-velocity component at 500 ms. KV model, (a) without and (b) with N-PML absorbers. Zener model, (c) without and (d) with N-PML absorbers. The dashed yellow lines indicate the boundaries in the absorbing strips. The numerical scheme is (2,∞) accurate (the pseudospectral method).

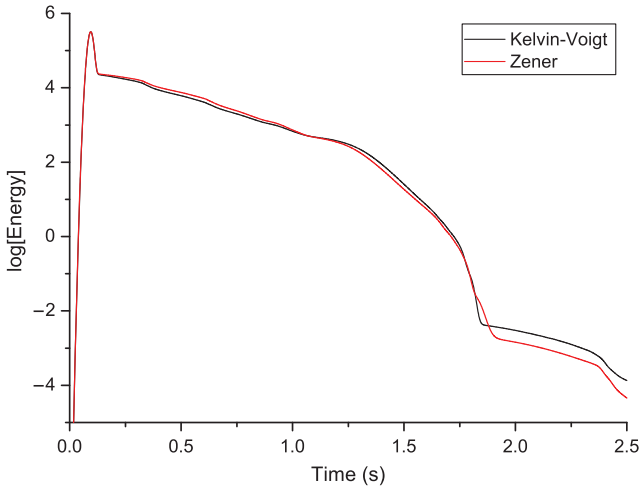

Figure 15. Decay of the total energy with time for the pseudospectral method.

case, $dt = 0.5$ ms. The same plots as in Figures 5 and 6 are shown in Figures 14 and 15. Without the ABC, wraparound can clearly be seen, whereas applying the N-PML ABC, these artifacts are effectively attenuated. The application of the N-PML ABC in pseudospectral modeling achieves equally satisfactory performance as in the FD simulation, as can be deduced from Figure 15, which shows the decay of the total energy with propagation time.

CONCLUSION

We have shown how to implement the N-PML absorber in anelastic forward modeling, illustrated with two mechanical models, namely, the KV and Zener constitutive equations. Although viscoelasticity is described by memory variables in the Zener case, similar artificial memory variables are used in the absorbing strips to damp the wavefield. The wave equations are solved with an FD method (16th-order in space) and with the pseudospectral method. The simulations show that the proposed equations effectively attenuate the field at the boundaries, either reflections or wraparound. The N-PML absorber exhibits a comparable accuracy as the C-PML one, involving fewer auxiliary variables and ordinary differential equations in the simulation of KV viscoelastic wave equation, and it is therefore more efficient computationally.

ACKNOWLEDGMENTS

This work has been supported by the "National Nature Science Foundation of China (grant no. 41804095)", the "Fundamental Research Funds for the Central Universities (grant no. 2019B17614)", and the "China Postdoctoral Science Foundation (grant no. 2017M621618 and 2019T120384)".

DATA AND MATERIALS AVAILABILITY

Data associated with this research are available and can be obtained by contacting the corresponding author.

APPENDIX A

SECOND-ORDER FD SCHEME

Let us consider the Zener equations and denote the time by $t = ndt$, where dt is the time step. The algorithm proceeds as follows at each time step:

1) Compute $\partial w_{xx}/\partial x$, $\partial w_{zz}/\partial z$ and $\bar{\vartheta} = \partial w_{xx}/\partial x + \partial w_{zz}/\partial z$. Then, we update e_1 as

$$e_1^{n+1} = \frac{[1 - dt/(2\tau_\sigma^{(1)})]e_1^n + dt(1/\tau_\epsilon^{(1)} - 1/\tau_\sigma^{(1)})\bar{\vartheta}}{1 + dt/(2\tau_\sigma^{(1)})}, \quad \text{(A-1)}$$

and e_2 with a similar equation (see equations 37 and 38).

2) Update τ_{xx} as

$$\begin{aligned}(1 + d_x dt/2)\tau_{xx}^{n+1} &= (1 - d_x dt/2)\tau_{xx}^n + \lambda dt\bar{\vartheta} \\ &+ 2\mu dt(\partial w_{xx}/\partial x) + \lambda dt(e_1^n + e_1^{n+1})/2 \\ &+ \mu dt(e_1^n + e_1^{n+1} + e_2^n + e_2^{n+1})/2, \end{aligned} \quad \text{(A-2)}$$

and τ_{zz} with a similar equation (see equation 40).

3) Update σ_{xx} as

$$\begin{aligned}\sigma_{xx}^{n+1} = \sigma_{xx}^n + \lambda dt\bar{\vartheta} + 2\mu dt(\partial w_{xx}/\partial x) + \lambda dt(e_1^n + e_1^{n+1})/2 \\ + \mu dt(e_1^n + e_1^{n+1} + e_2^n + e_2^{n+1})/2, \end{aligned} \quad \text{(A-3)}$$

and σ_{zz} with a similar equation (see equations 34 and 35).

4) Compute $\partial w_{xz}/\partial x$, $\partial w_{zx}/\partial z$ and update e_3:

$$e_3^{n+1} = \frac{[1 - dt/(2\tau_\sigma^{(2)})]e_3^n + dt(1/\tau_\epsilon^{(2)} - 1/\tau_\sigma^{(2)})(\partial w_{xz}/\partial x + \partial w_{zx}/\partial z)}{1 + dt/(2\tau_\sigma^{(2)})} \quad \text{(A-4)}$$

(see equation 39).

5) Update τ_{xxz} as

$$\begin{aligned}(1 + d_x dt/2)\tau_{xxz}^{n+1} &= (1 - d_x dt/2)\tau_{xxz}^n \\ &+ \mu dt(\partial w_{xz}/\partial x + \partial w_{zx}/\partial z) \\ &+ \mu dt(e_3^n + e_3^{n+1})/2, \end{aligned} \quad \text{(A-5)}$$

and τ_{zxz} with a similar equation (see equations 40).

6) Update σ_{xz} (see equation 36) similarly to step (3).

7) Compute $\partial\tau_{xx}/\partial x$, $\partial\tau_{zxz}/\partial z$, $\partial\tau_{xxz}/\partial x$ and $\partial\tau_{zz}/\partial z$, and update w_{xx}, w_{zx}, w_{zz}, w_{xz} as

$$w_{xx}^{n+1/2} = \frac{(1 - d_x dt/2)w_{xx}^{n-1/2} + (dt/\rho)(\partial\tau_{xx}/\partial x + \partial\tau_{zxz}/\partial z + f_x)}{1 + d_x dt/2}, \quad \text{(A-6)}$$

$$w_{zx}^{n+1/2} = \frac{(1 - d_z dt/2)w_{zx}^{n-1/2} + (dt/\rho)(\partial\tau_{xx}/\partial x + \partial\tau_{zxz}/\partial z + f_x)}{1 + d_z dt/2}, \quad \text{(A-7)}$$

$$w_{zz}^{n+1/2} = \frac{(1-d_z dt/2)w_{zz}^{n-1/2} + (dt/\rho)(\partial\tau_{xxz}/\partial x + \partial\tau_{zz}/\partial z + f_z)}{1+d_z dt/2}, \tag{A-8}$$

$$w_{xz}^{n+1/2} = \frac{(1-d_x dt/2)w_{xz}^{n-1/2} + (dt/\rho)(\partial\tau_{xxz}/\partial x + \partial\tau_{zz}/\partial z + f_z)}{1+d_x dt/2} \tag{A-9}$$

(see equation 40).

8) Update v_x and v_z using equation 20.

REFERENCES

Bécache, E., D. Givoli, and T. Hagstrom, 2010, High-order absorbing boundary conditions for anisotropic and convective wave equations: Journal of Computational Physics, **229**, 1099–1129, doi: 10.1016/j.jcp.2009.10.012.

Bérenger, J. P., 1994, A perfectly matched layer for the absorption of electromagnetic waves: Journal of Computational Physics, **114**, 185–200, doi: 10.1006/jcph.1994.1159.

Bodet, L., A. Dhemaied, R. Martin, R. Mourgues, F. Rejiba, and V. Tournat, 2014, Small-scale physical modeling of seismic-wave propagation using unconsolidated granular media: Geophysics, **79**, no. 6, T323–T339, doi: 10.1190/geo2014-0129.1.

Carcione, J. M., 1999, Staggered mesh for the anisotropic and viscoelastic wave equation: Geophysics, **64**, 1863–1866, doi: 10.1190/1.1444692.

Carcione, J. M., 2014, Wave fields in real media: Wave propagation in anisotropic, anelastic, porous and electromagnetic media, 3rd ed.: Elsevier, Handbook of Geophysical Exploration, (revised and extended).

Carcione, J. M., and H. B. Helle, 2004, On the physics and simulation of wave propagation at the ocean bottom: Geophysics, **69**, 825–839, doi: 10.1190/1.1759469.

Carcione, J. M., and D. Kosloff, 2013, Representation of matched-layer kernels with viscoelastic mechanical models: International Journal of Numerical Analysis and Modeling, **10**, 221–232.

Carcione, J. M., F. Poletto, and D. Gei, 2004, 3-D wave simulation in anelastic media using the Kelvin-Voigt constitutive equation: Journal of Computational Physics, **196**, 282–297, doi: 10.1016/j.jcp.2003.10.024.

Chen, J., 2011, Application of the nearly perfectly matched layer for seismic wave propagation in 2D homogeneous isotropic media: Geophysical Prospecting, **59**, 662–672, doi: 10.1111/j.1365-2478.2011.00949.x.

Chen, J., 2012, Nearly perfectly matched layer method for seismic wave propagation in poroelastic media: Canadian Journal of Exploration Geophysics, **37**, 22–27

Etienne, V., E. Chaljub, J. Virieux, and N. Glinsky, 2010, An hp-adaptive discontinuous Galerkin finite-element method for 3-D elastic wave modeling: Geophysical Journal International, **183**, 941–962, doi: 10.1111/j.1365-246X.2010.04764.x.

Hagstrom, T., E. Bécache, D. Givoli, and K. Stein, 2012, Complete radiation boundary conditions for convective waves: Communications in Computational Physics, **11**, 610–628, doi: 10.4208/cicp.231209.060111s.

Hu, W., A. Abubakar, and T. M. Habashy, 2007, Application of the nearly perfectly matched layer in acoustic wave modeling: Geophysics, **72**, no. 5, SM169–SM175, doi: 10.1190/1.2738553.

Hu, W., and S. A. Cummer, 2004, The nearly perfectly matched layer is a perfectly matched layer: IEEE Antennas and Wireless Propagation Letters, **3**, 137–140, doi: 10.1109/LAWP.2004.831077.

Komatitsch, D., and R. Martin, 2007, An unsplit convolutional perfectly matched layer improved at grazing incidence for the seismic wave equation: Geophysics, **72**, no. 5, SM155–SM167, doi: 10.1190/1.2757586.

Kosloff, D., and R. Kosloff, 1986, Absorbing boundaries for wave propagation problems: Journal of Computational Physics, **63**, 363–376, doi: 10.1016/0021-9991(86)90199-3.

Krawczyk, C. M., M. L. Buddensiek, O. Oncken, and N. Kukowski, 2013, Seismic imaging of sandbox experiments — Laboratory hardware setup and first reflection seismic sections: Solid Earth, **4**, 93–104, doi: 10.5194/se-4-93-2013.

Lai, C., and S. E. Minkoff, 2017, Nearly perfectly matched layer boundary conditions for operator upscaling of the acoustic wave equation: Computional Geosciences, **21**, 359–372, doi: 10.1007/s10596-017-9616-5.

Liu, Y., and M. K. Sen, 2010, A hybrid scheme for absorbing edge reflections in numerical modeling of wave propagation: Geophysics, **75**, no. 2, A1–A6, doi: 10.1190/1.3295447.

Liu, Y., and M. K. Sen, 2012, A hybrid absorbing boundary condition for elastic staggered-grid modeling: Geophysical Prospecting, **60**, 1114–1132, doi: 10.1111/j.1365-2478.2011.01051.x.

Martin, R., and D. Komatitsch, 2009, An unsplit convolutional perfectly matched layer technique improved at grazing incidence for the viscoelastic wave equation: Geophysical Journal International, **179**, 333–344, doi: 10.1111/j.1365-246x.2009.04278.x.

Oprsal, I., and J. Zahradnik, 1999, From unstable to stable seismic modeling by finite-difference method: Physics and Chemistry of the Earth. Part A: Solid Earth and Geodesy, **24**, 247–252, doi: 10.1016/S1464-1895(99)00026-5.

Rabinovich, D., D. Givoli, and E. Bécache, 2010, Comparison of high-order absorbing boundary conditions and perfectly matched layers in the frequency domain: International Journal for Numerical Methods in Biomedical Engineering, **26**, 1351–1369, doi: 10.1002/cnm.1394.

Ren, Z., and Y. Liu, 2013, A hybrid absorbing boundary condition for frequency-domain finite-difference modeling: Journal of Geophysics and Engineering, **10**, 054003, doi: 10.1088/1742-2132/10/5/054003.

Virieux, J., 1986, P-SV wave propagation in heterogeneous media: Velocity-stress finite-difference method: Geophysics, **51**, 889–901, doi: 10.1190/1.1442147.